J. Fluid Mech. (2006), *vol.* 567, *pp.* 399–414.
doi:10.1017/S0022112006002497 Printed in the United Kingdom

Numerical study of viscous modes in a rotating spheroid

By D. SCHMITT

LGIT, CNRS-UJF, BP 53, 38041 Grenoble Cédex 9, France
Denys.Schmitt@obs.ujf-grenoble.fr

(Received 18 November 2005 and in revised form 30 May 2006)

The motion of an incompressible viscous rotating fluid in an oblate spheroidal container is studied by direct numerical simulation in an appropriate spheroidal coordinate system and in the linear approximation. The behaviour of a few eigenmodes is investigated as a function of the eccentricity e of the container, for Ekman number $E = 10^{-5}$. Viscous effects are shown through internal shear layers, the spatial structure of which strongly depends on the eccentricity. In particular, for the spin-over mode, a resonance occurs around a critical value $e_c \approx 0.50$, where the decay rate deviates strongly from the predicted theoretical variation. This resonance is discussed in relation to the accidental coincidence between the spin-over frequency and two other frequencies corresponding to the (8,1,5) and (14,1,9) inertial eigenmodes.

1. Introduction

Understanding the dynamics of rotating fluids is of fundamental interest from a geophysical and astrophysical point of view. For the geodynamo problem the behaviour of inertial modes of the liquid inner core of the Earth in the presence of external constraints such as the ellipticity of its outer boundary and the precession forcing should be carefully investigated. The spheroidal geometry of this outer boundary was considered explicitly by Poincaré (Poincaré 1910), who found different effects on the Earth's nutation compared to the case of a spherical container, but viscosity was neglected. Viscosity was later considered as a perturbation of the non-viscous modes, with special attention given to the critical regions of the Ekman layer (Busse 1968; Greenspan 1968; Stewartson & Roberts 1963). In particular, the viscous correction to the decay rate and eigenfrequency for the spin-over mode was given analytically as a function of the ellipticity of the container. This was recently generalized for any inertial wave mode (Liao, Zhang & Earnshaw 2001; Zhang, Liao & Earnshaw 2004).

Following these fundamental analytical approaches, numerical studies have been undertaken in a sphere or a spherical shell (Hollerbach & Kerswell 1995; Noir, Jault & Cardin 2001; Rieutord & Valdaretto 1997; Tilgner & Busse 2001). Such simulations are needed to further our knowledge of the phenomena and to explain experimental results where fluid instabilities and turbulence are observed and reveal nonlinear effects. In particular, inertial modes are suspected to play a role in the geodynamo, because some of them could be destabilized by the elliptic shape of the boundaries due to the tides (Kerswell 1994).

Most of the numerical studies of rotating fluids have been in a spherical geometry, because of its relative simplicity. Using a more realistic coordinate system appears

highly desirable however, because natural bodies or cavities are often ellipsoidal rather than spherical. Such an approach has been used for studying kinematic dynamo models in a spheroidal galaxy (Walker & Barenghi 1994). More recently, a spheroidal symmetry has been considered for some geophysical applications (Lorenzani & Tilgner 2001, 2003; Tilgner 1999). In the latter approach, a coordinate transformation was performed in order to replace the ellipsoidal volume by a spherical one, for which a distorted equation of motion was used. A solid inner core was also included, to avoid singularities at the centre.

In the present work, the equation of motion of a rotating viscous incompressible fluid within a spheroidal container is directly treated in real space by using an appropriate set of coordinates, namely the oblate spheroidal coordinate system. Within this system, an extension of the spherical Mie representation of a vector field (Backus, Parker & Constable 1996) is considered: a solenoidal vector field (here the velocity field) is decomposed into the sum of two unique vectors which are themselves derived from two scalar fields, namely the sphero-poloidal and the sphero-toroidal ones. Similarly to the spherical symmetry, this Mie-like representation allows one to work with only two scalar fields instead of the three velocity components, once the pressure has been eliminated from the equations. In addition, an appropriate spherical harmonic expansion is used for the angular part of these spheroidal scalar fields, while a discretization is performed for their sphero-radial component. The main features of this formalism have been previously presented in detail, but only a few preliminary numerical results were included (Schmitt & Jault 2004). Here, numerical simulations are performed more thoroughly. In particular, the behaviour of a few viscous eigenmodes is investigated as a function of eccentricity and, to a lesser extent, of viscosity. Their spatial geometry is discussed, exhibiting features which suggest the presence of possible resonance between them, under certain circumstances.

In the present work, the linear approximation is made, and no inner core is considered. In § 2, the mathematical formalism within the oblate spheroidal coordinate system is briefly recalled, and two distinct procedures are described to solve the equation of motion, namely a time-stepping and an inverse iteration method. Section 3 is devoted to the numerical results of a systematic study of a particular mode, i.e. the spin-over mode, as a function of the excentricity and for Ekman number $E = 10^{-5}$, showing the presence of a resonance around a critical eccentricity $e_c = 0.50$. This behaviour differs markedly from what was expected from previous theoretical approaches. In § 4, the behaviour of the other spheroidal viscous eigenmodes is considered and their role in the occurence of the spin-over resonance is discussed. The last Section is devoted to a discussion.

2. Mathematical formalism

2.1. *The oblate spheroidal coordinate system*

A coordinate system particularly appropriate to the present study (spheroidal container, no inner core) is the oblate spheroidal system, related to the Cartesian one by the relations

$$\left.\begin{array}{l} x = a\cosh\mu\ \sin\theta\ \cos\varphi \\ y = a\cosh\mu\sin\theta\sin\varphi \\ z = a\sinh\mu\cos\theta \end{array}\right\} \quad \text{with } \mu \geqslant 0,\ 0 \leqslant \theta \leqslant \pi,\ 0 \leqslant \varphi < 2\pi, \tag{2.1}$$

where a is the distance between the origin and the circle of foci within the equatorial plane. Within this system, the constant-μ surfaces are ellipsoids with eccentricity

$e = 1/\cosh\mu$, while the constant-θ surfaces are one-sheet hyperboloids which, for large μ values, become asymptotically cones of revolution around the z-axis with a half-aperture θ. Details of the formalism can be found in Schmitt & Jault (2004), and only a summary is given below, including some changes to the previous work.

2.2. *Decomposition of scalar and vectorial fields in the spheroidal symmetry*

As shown by Schmitt & Jault (2004), an appropriate transformation allows one to expand any scalar function $f(\mu, \theta, \varphi)$ within the usual spherical harmonics basis $Y_l^m(\theta, \varphi)$, where θ is the spheroidal, not the spherical colatitude. In the same way, a solenoidal vector field $\boldsymbol{V}(\mu, \theta, \varphi)$ can be decomposed into the sum of a sphero-toroidal $\mathbf{V}_{st}$ and a sphero-poloidal $\boldsymbol{V}_{sp}$ part, with

$$\left.\begin{aligned} \boldsymbol{V}_{st} &= \nabla \times \left(\frac{a}{4\sqrt{\sinh^2\mu + \cos^2\theta}} st\, \hat{\boldsymbol{e}}_\mu \right), \\ \boldsymbol{V}_{sp} &= \nabla \times \left(\frac{1}{2\sin\theta\sqrt{\sinh^2\mu + \cos^2\theta}} \hat{\boldsymbol{e}}_\theta \partial_\varphi sp - \frac{1}{2\cosh\mu} \hat{\boldsymbol{e}}_\varphi \partial_\theta sp \right), \end{aligned}\right\} \tag{2.2}$$

where ∂_α stands for ∂/∂_α, and $st(\mu, \theta, \varphi)$ and $sp(\mu, \theta, \varphi)$ are the sphero-toroidal and sphero-poloidal scalar fields of $\boldsymbol{V}$, respectively. This decomposition ensures the vanishing of $\nabla \cdot \boldsymbol{V}$, in agreement with the incompressibility of the fluid. Note that differences exist compared to the Mie decomposition in spherical symmetry, for example the curl of a sphero-poloidal vectorial field is not a sphero-toroidal field, nor vice versa.

2.3. *Equation of motion*

The present work is focused on the study of the viscous correction to inviscid eigenmodes in the linear approximation. An incompressible fluid of viscosity ν is enclosed in an oblate spheroidal container of sphero-radial coordinate μ_o and eccentricity $e_o = 1/\cosh\mu_o$. The container is spinning at frequency ω_o around the z-axis. The linear dimensionless equation of motion for the fluid velocity $\boldsymbol{u}$ within the coordinate system rotating with the container is

$$\partial_t \boldsymbol{u} + 2\hat{\boldsymbol{z}} \times \boldsymbol{u} = -\nabla\phi + \frac{E}{e_o^2} \Delta \boldsymbol{u} \tag{2.3}$$

where ϕ is the reduced pressure and $E = \nu\omega_o^{-1}(a\cosh\mu_o)^{-2}$ the Ekman number. Here the focus parameter a has been taken as unit of length, and ω_o^{-1} as unit of time.

After eliminating the pressure by taking the curl of equation (2.3), three coupled differential equations can be obtained for the two unknown quantities $st(\mu, \theta, \varphi)$ and $sp(\mu, \theta, \varphi)$ after projection on the three basis vectors $\hat{\boldsymbol{e}}_\mu, \hat{\boldsymbol{e}}_\theta, \hat{\boldsymbol{e}}_\varphi$. Note that these three equations are not independent, and this will be used below to reduce the order of μ-derivatives. These equations involve μ-derivatives up to the fourth order, and θ- and φ-derivatives up to the fifth order. Note that the φ-derivate is straightforward to obtain when the spherical harmonic expansion is considered, while the order of the θ-derivatives can be reduced to first order by using the angular Laplacian operator. After some manipulation, the θ-dependence includes numerous terms such as $\cos^n\theta$ or $\cos^{n-1}\theta\sin\theta\partial_\theta$, where n can be as large as 7, but no high-order θ-derivative. For μ-derivatives, a careful examination of the boundary conditions (see § 2.4) one reveals that needs to keep at most fourth-order derivatives for $sp(\mu, \theta, \varphi)$ and second-order derivatives for $st(\mu, \theta, \varphi)$, a condition which is fulfilled for the μ-equation. However, as both θ- and φ-equations involve $\partial_\mu^3 st(\mu, \theta, \varphi)$, an appropriate combination of

them has been considered so that this term can be cancelled. For conciseness, the two remaining μ- and (θ, φ)-equations are not given here.

The next step is to use the spherical harmonic expansion for both scalar fields $st(\mu, \theta, \varphi)$ and $sp(\mu, \theta, \varphi)$. Thus, the θ-dependent operators quoted above, e.g. $\cos^n \theta$, when applied to a function Y_l^m, can be expanded into the sum of $(n+1)$ spherical harmonics with the same order m, and same degrees of parity ranging from $l-n$ to $l+n$. The system of equations can then be reduced to expressions which involve partial derivatives in μ and t only, and are expanded in spherical harmonics. Finally, considering separately each angular part l provides a set of coupled equations which include numerous contributions from terms with other angular parts up to $\Delta l = 7$ (i.e. from $l-7$ to $l+7$). All the expressions have been derived using Mathematica software.

2.4. *Boundary conditions*

The no-slip condition has been used at the outer boundary of the container, i.e. $\boldsymbol{u}(\mu_o) = 0$. This leads to the following relations:

$$st_l^m(\mu_o) = 0, \quad sp_l^m(\mu_o) = 0, \quad \partial_\mu sp_l^m(\mu_o) = 0, \tag{2.4}$$

where $sp_l^m(\mu)$ and $st_l^m(\mu)$ are the spherical harmonic expansion coefficients of the sp and st scalar fields. A second set of relations comes from the critical disk $\mu = 0$ enclosed by the focal circle. The absence of an inner core implies that $\boldsymbol{u}$ and its derivatives are continuous when passing through this surface, the two sides of this surface corresponding to θ and $\pi - \theta$. That leads to the following parity relations for the functions $st_l^m(\mu)$ and $sp_l^m(\mu)$ for small values of μ: $sp_l^m(\mu)$ and $st_l^m(\mu)$ must be odd if $(l+m)$ is even, and even if $(l+m)$ is odd. In the present calculation, this is equivalent to the vanishing of $st_{2n+1}^1(0)$, $\partial_\mu sp_{2n}^1(0)$, $\partial_\mu^3 sp_{2n}^1(0)$. Note that the choice of the latter term rather than $\partial_\mu^2 st_{2n+1}^1(0)$ comes from the following argument: if an inner core were used, the boundary condition would be the same as equation (2.4), but for $\mu = \mu_i$, i.e. one condition on $st_l^m(\mu_i)$ and two on $sp_l^m(\mu_i)$. Note that this choice remains consistent with the order of the derivatives of $st_l^m(\mu)$ and $sp_l^m(\mu)$ in the equation of motion, i.e. 2 and 4, respectively.

2.5. *Numerical methods*

Numerical calculations use the finite difference method for the sphero-radial variable μ. The grid is linear, except near the boundaries where it follows a geometric law: the grid is then extended near the critical disk $\mu = 0$ in order to reduce numerical problems near the focal circle, while it is compressed close to $\mu = \mu_o$ in order to increase the number of points within the Ekman boundary layer. The total number of points is generally taken as $N = 251$. For the angular variables, the spherical harmonic expansion is truncated at $l_{max} = 64$. For the azimutal part, only $(m = 1)$ terms are needed for the spin-over problem (see § 2.6), the $(m = -1)$ terms being related to the $(m = 1)$ one through complex conjugation.

The corresponding matrices consist of a block-pentadiagonal matrix associated with the radial grid, each block being a band-matrix of order l_{max}, arising from the coupling of scalar field components having different l values. Moreover, due to symmetry considerations, two independent groups of these components can be considered separately: the first group involves $sp_1^m, st_2^m, sp_3^m, st_4^m \ldots$, while the second one, which is used below, includes $st_1^m, sp_2^m, st_3^m, sp_4^m \ldots$.

For the time dependence, two different method have been considered. First, the implicit Crank–Nicolson scheme has been used for the diffusion term (initial value

problem). For each time step, inversion of the large pentadiagonal matrix is carried out by LU factorization and the Thomas algorithm, in order to avoid holding in the memory the inverse of this matrix. The LAPACK routines have been used for manipulating the matrices. In the second procedure the inverse iteration method has been applied (Stoer & Bulirsch 1980), which provides complex eigenvalues, i.e. both eigenfrequency and attenuation rate, as well as eigenvectors. The selection of the final eigenmode is made by starting the iterations from an initial complex eigenvalue close to the expected value. Any individual viscous eigenmodes can then be obtained by this procedure, but identifying the corresponding (n, m, k) labels may not be trivial, in particular for values of n not small. Moreover, the final eigenmode is generally not very sensitive to the imaginary part of the starting value, i.e. the initial attenuation rate, except when eigenvalues are close to each other. That may explain the presence of some irregularities in the calculated variations (see below). In the following, both methods have been used to study the spin-over behaviour, while other eigenmodes have been investigated only by the inverse iteration method.

2.6. *Description of the initial inviscid spin-over mode*

In the Crank–Nicolson scheme, an initial condition has to be taken as the starting ($t = 0$) velocity field. For the spin-over investigation, the choice is the (2,1,1) inviscid inertial (Poincaré) mode, for which all the components are purely linear in the spatial coordinates (x, y, z) and which satisfies the non-penetration condition on the spheroidal container boundary $\mu = \mu_o$ (Greenspan 1968; Kerswell 1993):

$$\boldsymbol{u}_{\mathbf{211}} = \frac{z}{\tanh(\mu_o)}\,\hat{\boldsymbol{e}}_y - \tanh(\mu_o) y \hat{\boldsymbol{e}}_z. \tag{2.5}$$

This mode corresponds to a vortical flow around the $\hat{\boldsymbol{e}}_x$-axis, with a constant vorticity and no boundary layer. This inviscid inertial mode is excited when fluid is in rapid rotation around the z-axis and its rotation axis is suddenly tilted by a small amount (Greenspan 1968). Precession may be viewed as a sequence of such infinitesimal changes so it is anticipated that this mode plays a key role in that problem. Writing equation (2.5) in the spheroidal coordinate system and expanding the corresponding scalar fields in spherical harmonics leads to only three non-zero terms which involve only $m = 1$ (see Schmitt & Jault 2004), namely st_1, sp_2, st_3 (here and in the following, the index $m = 1$ has been omitted for simplicity). Note that the boundary conditions are satisfied at $\mu = 0$ but not at $\mu = \mu_o$ for these three scalar fields. The values at $\mu_N = \mu_o$ for st_1 and st_3, as well as the previous one at μ_{N-1} for sp_2 need to be modified in order to fulfil the outer boundary conditions and to take into account the viscosity through equation (2.4). As will be seen below, a consequence of this abrupt change is to excite high-order viscous eigenmodes which will be visible in the time dependence shown below, giving rise to rapidly decaying transient oscillations.

2.7. *The angular momentum*

The expression for true vorticity in the spheroidal system being complex to evaluate, an alternative, simpler way to follow the evolution of the rotating fluid is to calculate its angular momentum ℓ, defined as (the prefactor has been removed)

$$\ell = \int_{spheroid} \boldsymbol{r} \times \boldsymbol{u}. \tag{2.6}$$

Within the spherical limit, this vector is in fact half of the true vorticity, $(1/2)\nabla \times \boldsymbol{u}$. In spheroidal symmetry, expanding the scalar fields of the velocity field $\boldsymbol{u}$ in spherical harmonics and integrating their angular parts leads to an expression which involves

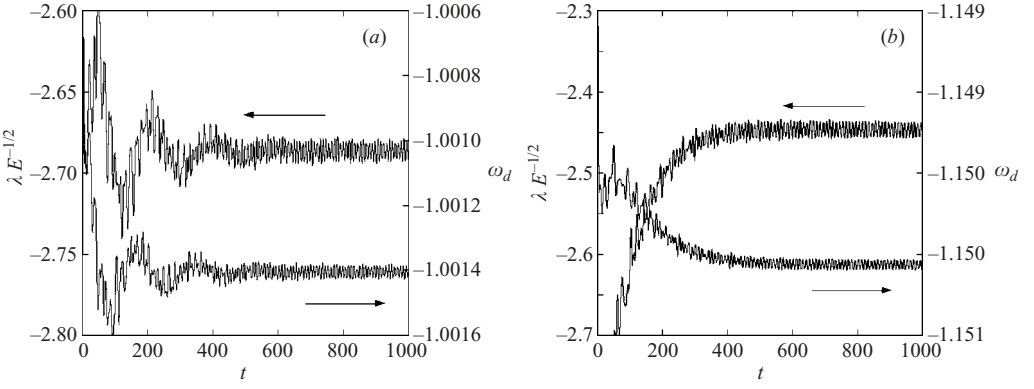

FIGURE 1. Calculated variation of renormalized decay factor $\lambda E^{-1/2}$ (left scale) and eigenfrequency ω_d (right scale) of the spin-over mode for eccentricities $e = 0.02$ (a) and 0.51 (b) and for Ekman number $E = 10^{-5}$.

only st_1 and sp_2. Moreover, it turns out that this angular momentum, apart a constant prefactor, is simply the projection of the vector field $\boldsymbol{u}$ on the two orthogonal inviscid spin-over modes $\boldsymbol{u}_{2\,1\,1}$ and $\boldsymbol{u}_{2\bar{1}\,1}$ which correspond to the inertial vortical flows around $\hat{\boldsymbol{e}}_x$ and $\hat{\boldsymbol{e}}_y$, respectively:

$$\ell = -\coth(2\mu_o)\left[\int_{spheroid}(\boldsymbol{u}^*_{2\,1\,1}\cdot\boldsymbol{u})\hat{\boldsymbol{e}}_x + \int_{spheroid}(\boldsymbol{u}^*_{2\bar{1}\,1}\cdot\boldsymbol{u})\hat{\boldsymbol{e}}_y\right]. \tag{2.7}$$

The evolution of the system will be followed by investigating the time-variation of this vector ℓ, which remains confined within the equatorial plane, as well as its dependence on viscosity and eccentricity.

3. Numerical results

3.1. *Time dependence of the decay factor and eigenfrequency*

The angular momentum ℓ can be defined by its modulus l_{mod} and its position. From a theoretical point of view, l_{mod} is expected to decay exponentially with time owing to viscous effects (negative decay factor λ), while the vector ℓ is expected to rotate in the equatorial plane in a retrograde way (negative angular speed ωd):

$$\left.\begin{aligned} l_{mod} &= l_0\exp(\lambda t),\\ (\ell, \hat{\boldsymbol{e}}_x) &= \pi + \omega_d t,\end{aligned}\right\} \tag{3.1}$$

where $(\ell, \hat{\boldsymbol{e}}_x)$ is the angle between vectors ℓ and $\hat{\boldsymbol{e}}_x$. At each time step, the decay factor is then calculated as $\mathrm{d}(l_{mod})/l_{mod}$ and the angular speed as $\mathrm{d}(\ell, \hat{\boldsymbol{e}}_x)/\mathrm{d}t$. Two typical time dependences of these quantities are reported in figure 1 for Ekman number $E = 10^{-5}$, which shows the time-stepping procedure as well as the effects of ellipticity. After some long-period transient oscillations, a stationary state is reached for large t values, where residual small oscillations exist around a constant value for both decay rate λ and eigenfrequency ωd.

3.2. *Eccentricity dependence of the decay factor and eigenfrequency*

The eccentricity dependence of the large-t limit of the decay rate and eigenfrequency is reported in figure 2, together with the values calculated directly by the inverse iteration method. The two results are in perfect agreement, proving that the former are not

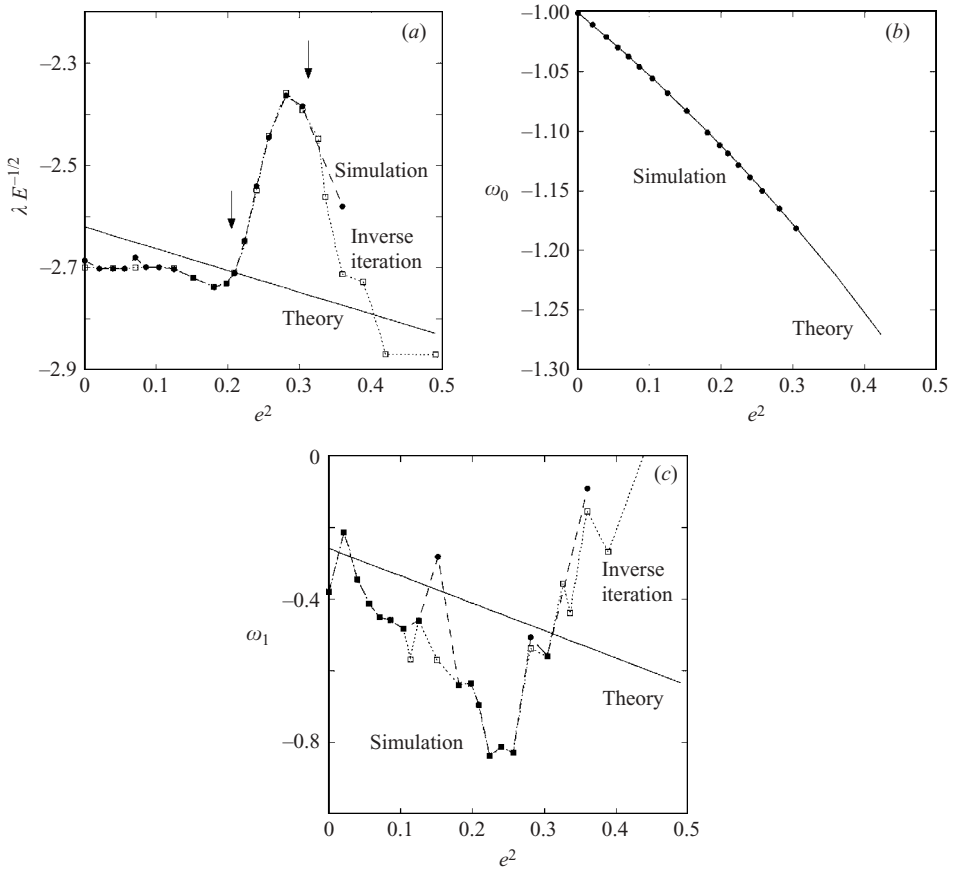

FIGURE 2. Eccentricity dependence of the renormalized decay factor $\lambda E^{-1/2}$ (*a*) and of ω_0 (*b*) and ω_1 (*c*) contributions to the eigenfrequency ω_d for the spin-over mode; continuous lines are theoretical predictions; dashed lines with circles correspond to the present time-stepping simulations and dotted lines with squares to inverse iteration results; arrows indicate the crossing between the spin-over frequency and the (8,1,5) and (14,1,9) frequencies, respectively.

affected much by the vanishing residual modes which still exist in the calculation for large t. In other words, the large-t limit is very close to the pure viscous spin-over eigenmode. These variations can be compared to those obtained according to the theoretically following relations (Greenspan 1968; Stewartson & Roberts 1963; Zhang *et al.* 2004):

$$\left.\begin{aligned} &\lambda = \lambda_1(e)E^{1/2} + O\big(E, e^4E^{1/2}\big),\\ &\omega_d = \omega_0(e) + \omega_1(e)E^{1/2} + \cdots,\\ &\text{with } \lambda_1(e) = -2.62 - 0.426\,e^2, \quad \omega_0(e) = \frac{-2}{2-e^2} \text{ and } \omega_1(e) = -0.258 - 0.766\,e^2. \end{aligned}\right\} \tag{3.2}$$

The renormalized decay rates and the eigenfrequencies are found to follow satisfactorily the predicted variation, at least for moderate eccentricities. The ω_1 variation is a little more erratic, but it is worth noting that this quantity is a high order one in the expansion of ω_d, therefore it is subject to a lower degree of accuracy. However, a spectacular change of behaviour clearly occurs around $e_c \approx 0.5$, emphasized by

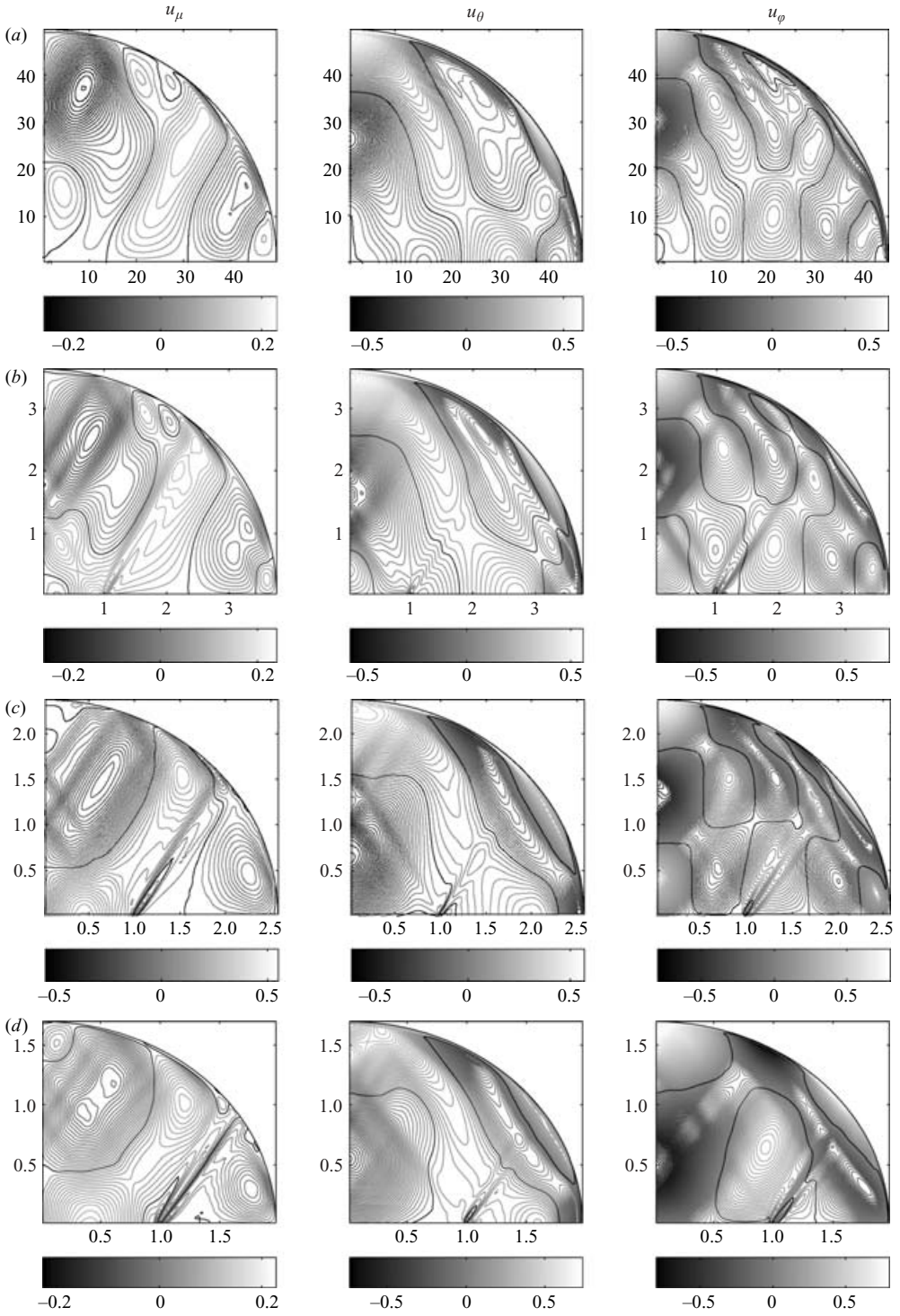

FIGURE 3. The three components of the residual fluid velocity of the (2,1,1) spin-over mode within the meridional plane containing the ℓ vector, for different eccentricities, after removing the inviscid contribution (see text); velocities are normalized so that $|\boldsymbol{u}|_{max} = 1$; note the spatial evolution of the azimutal component. (*a*) $e = 0.02$, (*b*) $e = 0.27$, (*c*) $e = 0.39$, (*d*) $e = 0.51$.

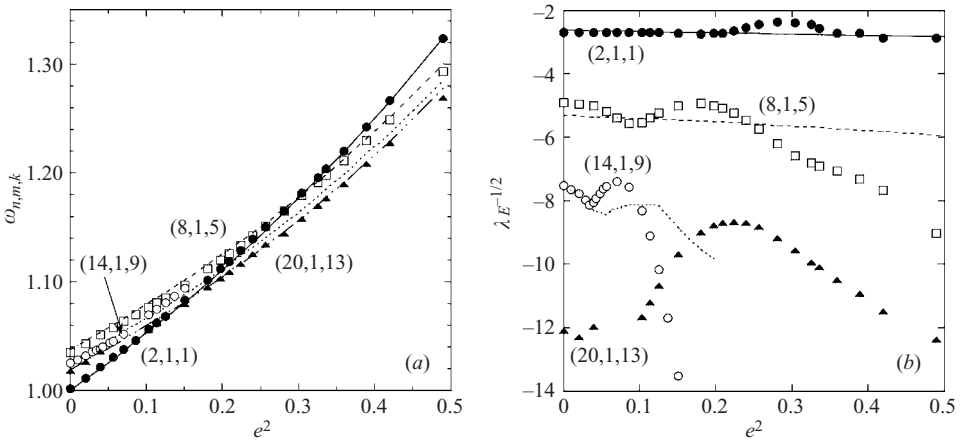

FIGURE 4. (*a*) Eccentricity dependence of eigenfrequencies, for some inviscid (lines) and viscous (symbols) spheroidal inertial modes close to the (2,1,1) spin-over mode. (*b*) Eccentricity dependence of corresponding decay rates. Continuous line and full circles: (2,1,1) mode; dashed line and open squares: (8,1,5) mode; dotted line and open circles: (14,1,9) mode; triangles and dashed dotted lines: (20,1,13) mode; lines are theoretical predictions.

the strong deviation of λ from the e^2 dependence. Unfortunately, the appearance of numerical instabilities for $e > 0.6$–0.7 prevents us from analysing the behaviour for higher eccentricities. In order to have a deeper understanding of what happens around this critical eccentricity, the spatial structure of the spin-over mode should be examined carefully in the presence of both viscosity and eccentricity.

3.3. *Spatial structure of the spin-over mode*

The detailed spatial structure of the flow resulting from the combined effect of the viscosity and the non-spherical shape of the container can be appreciated by subtracting an appropriate non-viscous spin-over contribution from the calculated viscous flow. The three components of the residual fluid velocity are then visualized within the meridional plane containing the rotation axis of the removed spin-over contribution or equivalently the ℓ vector itself (see figure 3). Note that the spatial structures calculated by the two methods are indistinguishable from each other. They exhibit shear regions, although the relatively high Ekman number limits the narrowness of the shear layers. The main characteristic feature is the spatial evolution of the azimutal component u_φ. While for $e = 0.02$ features are similar to those calculated by Hollerbach & Kerswell (1995) and Noir *et al.* (2001) in spherical geometry, the u_φ component exhibits more pronounced cells when e increases, reminiscent of some inviscid spheroidal inertial modes (see below). Nevertheless these structures are characteristic of the viscous spin-over eigenmode (2,1,1), so that explaining the presence of such features requires investigating in more detail the behaviour of the spheroidal inertial eigenmodes themselves and their dependence on viscosity and eccentricity.

4. The spheroidal inertial eigenmodes

4.1. *The non-viscous inertial modes*

First we focus on the non-viscous spheroidal inertial modes, which are plane wave solutions of equation (2.3) for $E = 0$. According to the notation of Kerswell (1993),

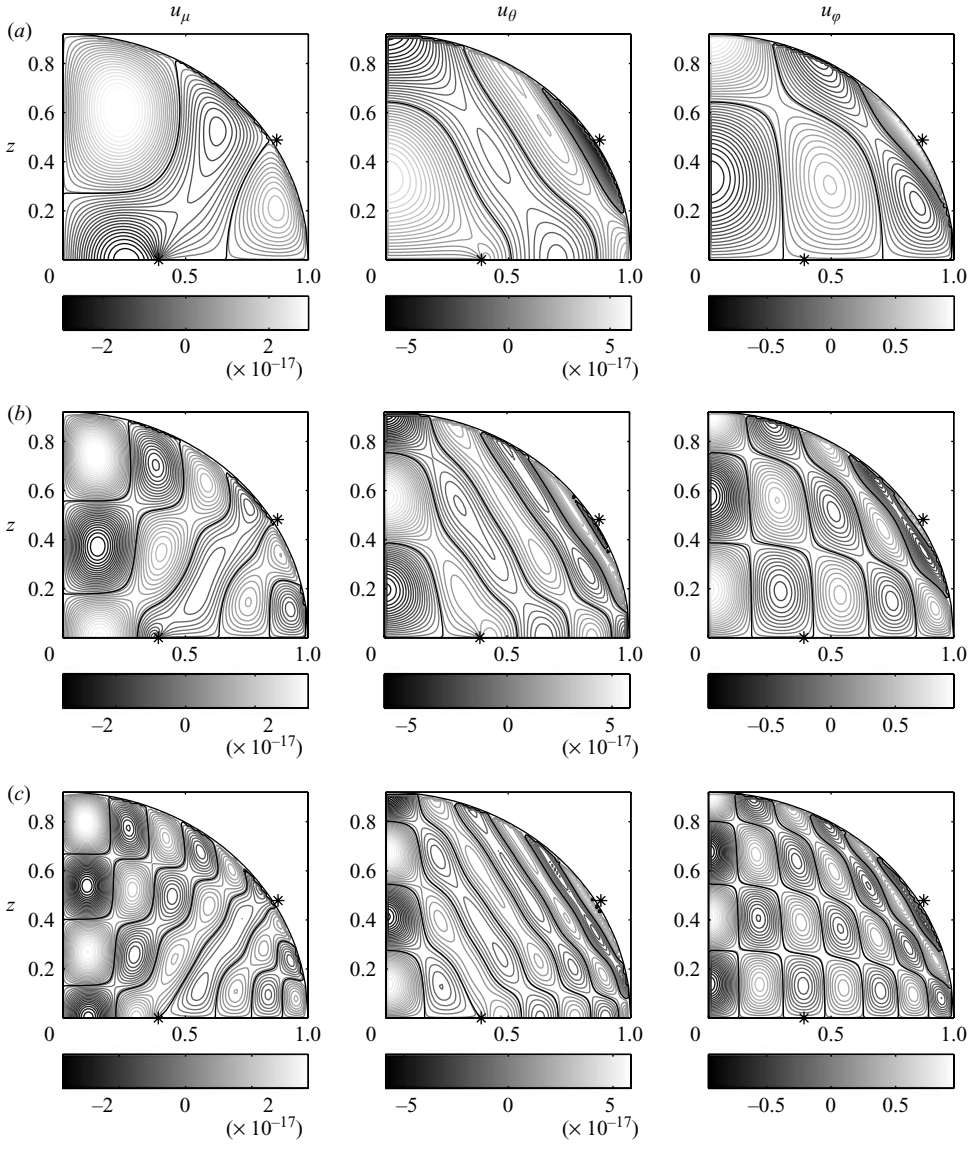

FIGURE 5. The three velocity components of the (*a*) (8,1,5), (*b*) (14,1,9) and (*c*) (20,1,13) inviscid inertial modes within the meridional plane $\varphi = 0$, for $e = 0.39$; velocities are normalized so that $|\boldsymbol{u}|_{max} = 1$; the critical latitude for viscous boundary layer eruptions is indicated by a star on the spheroidal boundary.

there are an infinite number of such eigenfunctions $Q_{n,m,k}$ (the Poincaré modes), depending on the three labels n, m, k:

$$Q_{n,m,k}(\mu, \theta, \varphi, t) = Q_{n,m,k}(\mu, \theta)\ \exp(\mathrm{i}(m\varphi + \omega_{n,m,k}t)) \tag{4.1}$$

where n and m refer to the associated Legendre polynomials P_n^m in the analytical expression of the eigenmodes and eigenfrequencies, while k labels the different eigenfrequencies $\omega_{n,m,k}$ corresponding to a given set of (n, m) values. These frequencies depend on the eccentricity e, as shown in figure 4(*a*) for a selection of eigenmodes,

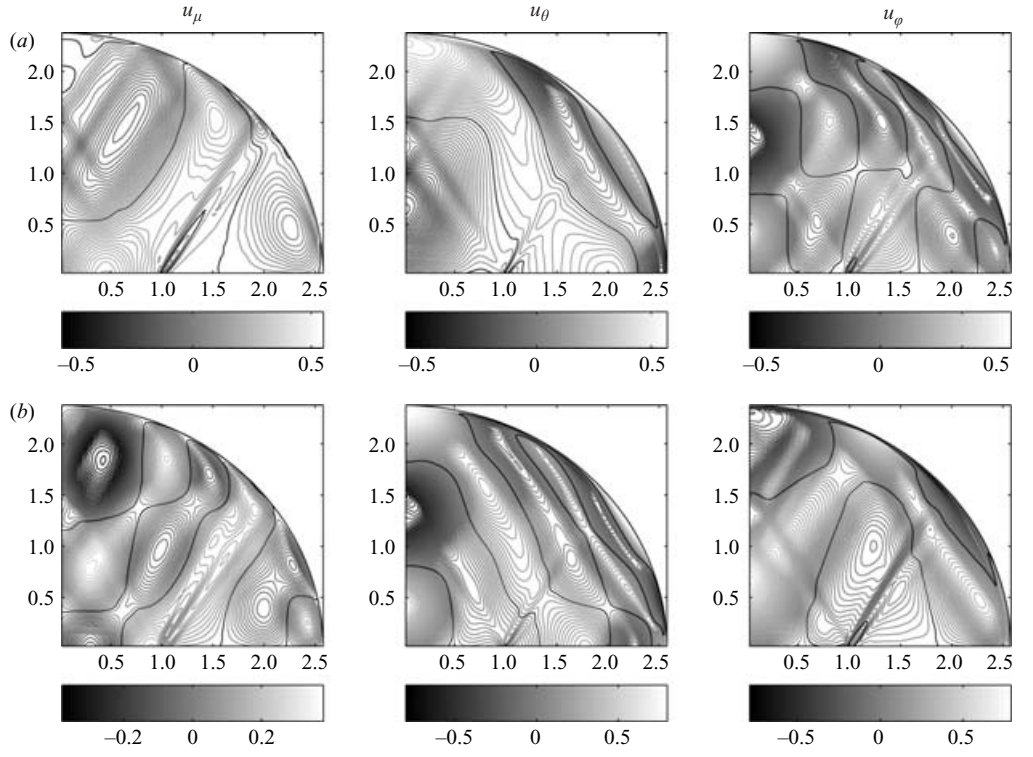

FIGURE 6. The three components of the residual fluid velocity of the (2,1,1) viscous spin-over mode ($\varphi = 0$) within the meridional plane containing the ℓ vector (a) and perpendicular to it ($\varphi = \pi/2$) (b), for $e = 0.39$.

the frequency of which is close to that of the spin-over one, $\omega_{2,1,1}$ (note that this is the same as ω_o of equation (3.2), except the sign), i.e. close to 1. Clearly the (8,1,5) and (14,1,9) modes are expected to play a particular role, and it is worth considering their spatial distribution (see figure 5 for $e = 0.39$ for example). Note that their global geometry is not very different for the spherical case, $e = 0$, and a noticeably oblate case, $e = 0.7$. While the non-viscous (2,1,1) mode always exhibits a very simple laminar structure – it looks like a stretched solid body rotation – the geometrical features of both (8,1,5) and (14,1,9) modes are very close to those present in the calculated viscous spin-over mode (see § 3.3). They are even both present in a single viscous eigenmode, if the azimuthal variation of the three components is considered (see figure 6 for $e = 0.39$). Therefore, it can be anticipated that a viscosity-induced resonance occurs between all three inertial modes, in the range of eccentricity where their frequencies cross. So it is interesting to investigate more thoroughly how the different inertial modes are affected by the viscosity.

4.2. *The viscous inertial modes*

Including viscosity in equation (2.3) prevents us from solving analytically the eigenproblem. In contrast, the inverse iteration method may allow viscous solutions to be obtained for different modes and an appreciation of how their eigenfrequency, decay rate and spatial structure are modified by the viscosity as a function of eccentricity. As seen in figure 4(a), the viscous eigenfrequencies generally agree well

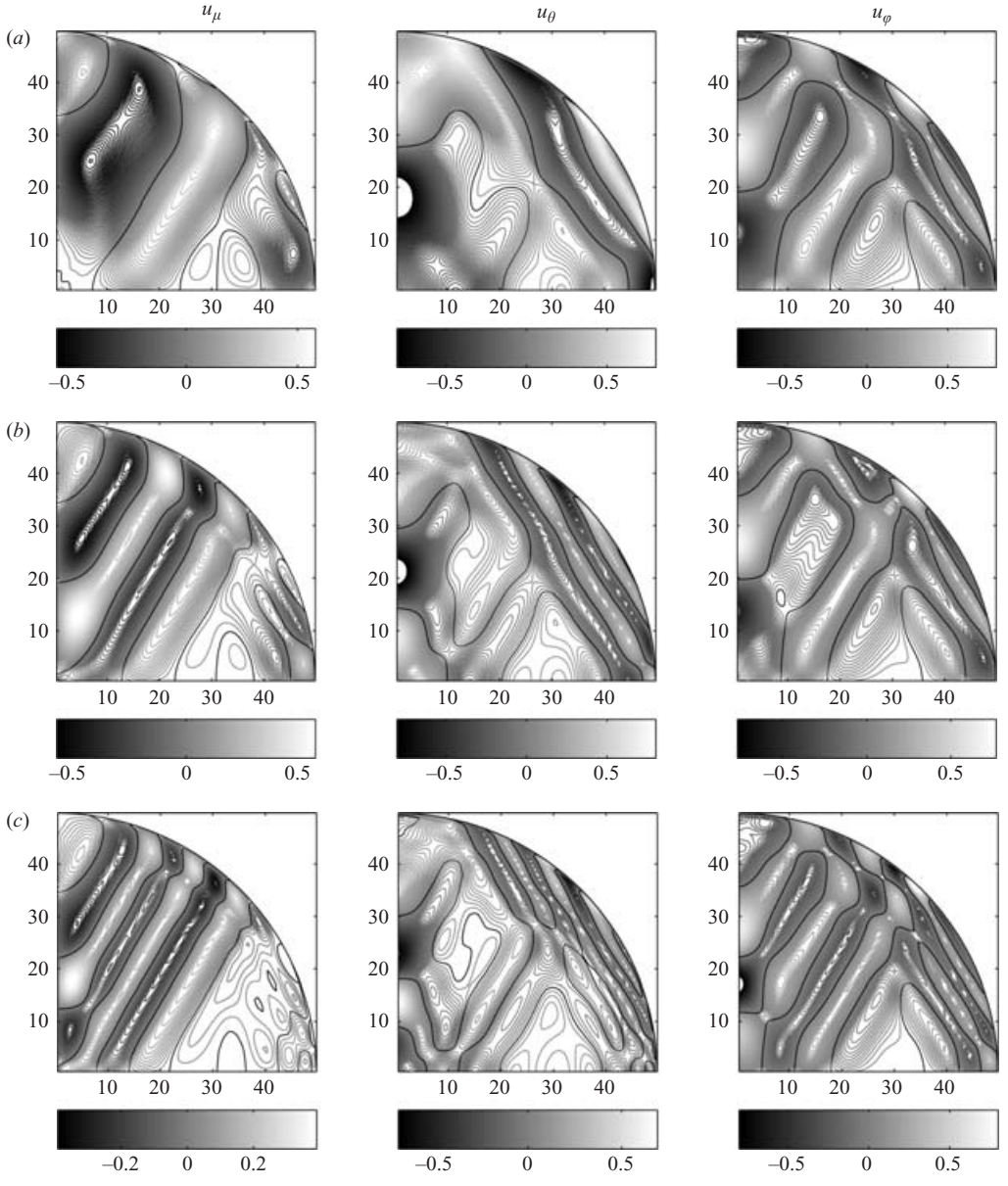

FIGURE 7. The three velocity components of the (8,1,5) (*a*), (14,1,9) (*b*) and (20,1,13) (*c*) viscous inertial modes within the meridional plane $\varphi = 0$, for $e = 0.02$; velocities are normalized so that $|\boldsymbol{u}|_{max} = 1$.

with the corresponding inviscid variation. Nevertheless, difficulties may sometimes occur when following some modes over the whole eccentricity range, for example the (14,1,9) mode for $e > 0.4$ or the (20,1,13) mode around $e \approx 0.3$. In these cases, the inverse iteration procedure converges toward an eigenmode corresponding to a much higher n value, whatever the starting point, at least in our range of investigation. It is worth noting that this procedure is indeed more efficient for well-separated eigenvalues, which is precisely not the case here. If the viscous decay rates are

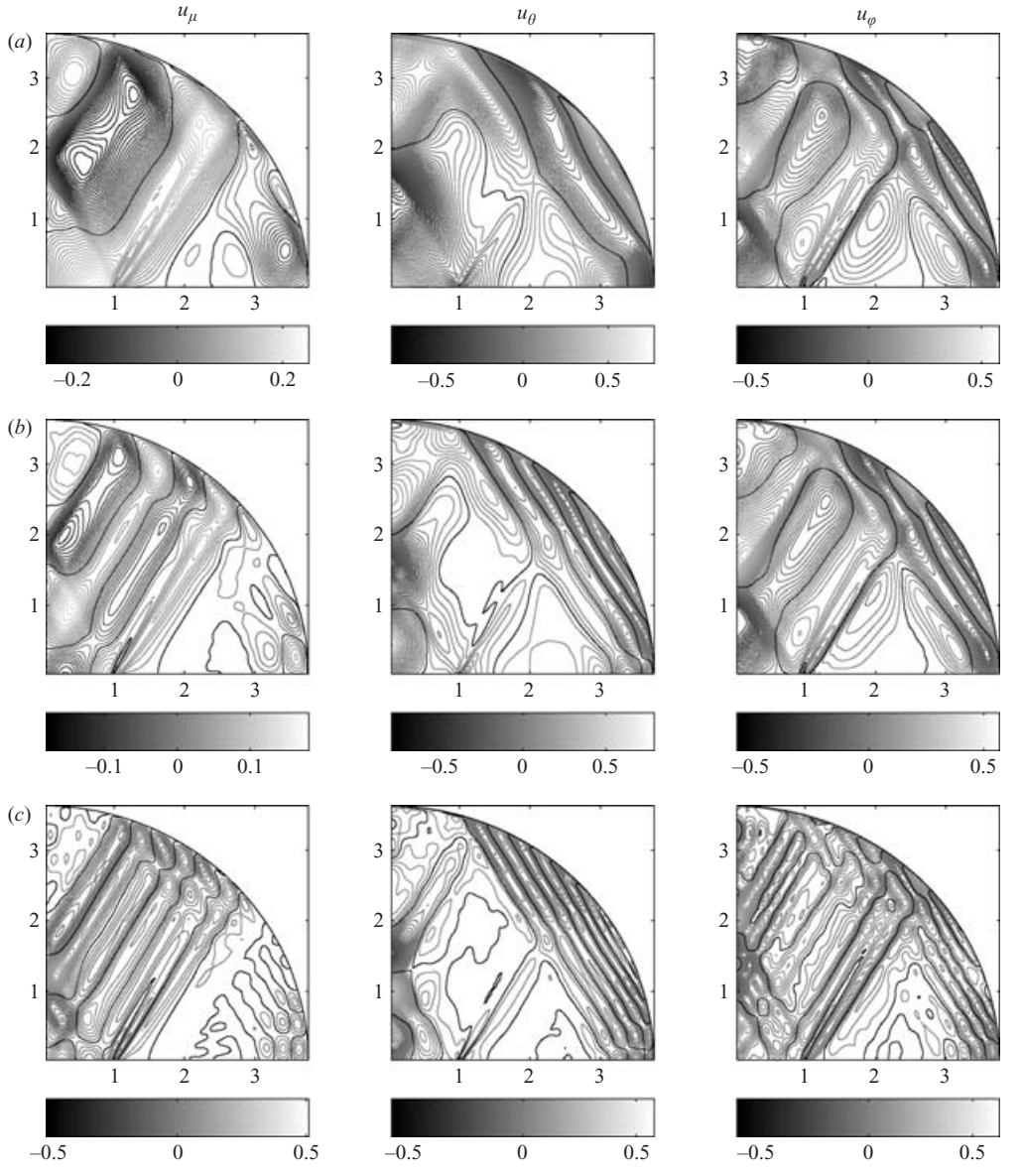

FIGURE 8. The three velocity components of the (8,1,5) (*a*), (14,1,9) (*b*) and (20,1,13) (*c*) viscous inertial modes within the meridional plane $\varphi = 0$, for $e = 0.27$; velocities are normalized so that $|\boldsymbol{u}|_{max} = 1$.

considered (see figure 4*b*), it is obvious that they do not follow a simple e^2 law, but exhibit anomalies reminiscent of the behaviour of the spin-over mode, or even seem to diverge, such as the (14,1,9) mode for $e > 0.4$.

The spatial distribution has been also obtained, as shown in figures 7–9 for the viscous (8,1,5), (14,1,9) and (20,1,13) modes, for three values of eccentricity. Surprisingly, the cell-like features seen in the corresponding non-viscous modes are less apparent in the presence of viscosity, where they are replaced by geometrical structures more reminiscent of shear layers. These features also make more difficult the identification of the modes found by the inverse iteration procedure. Resonance

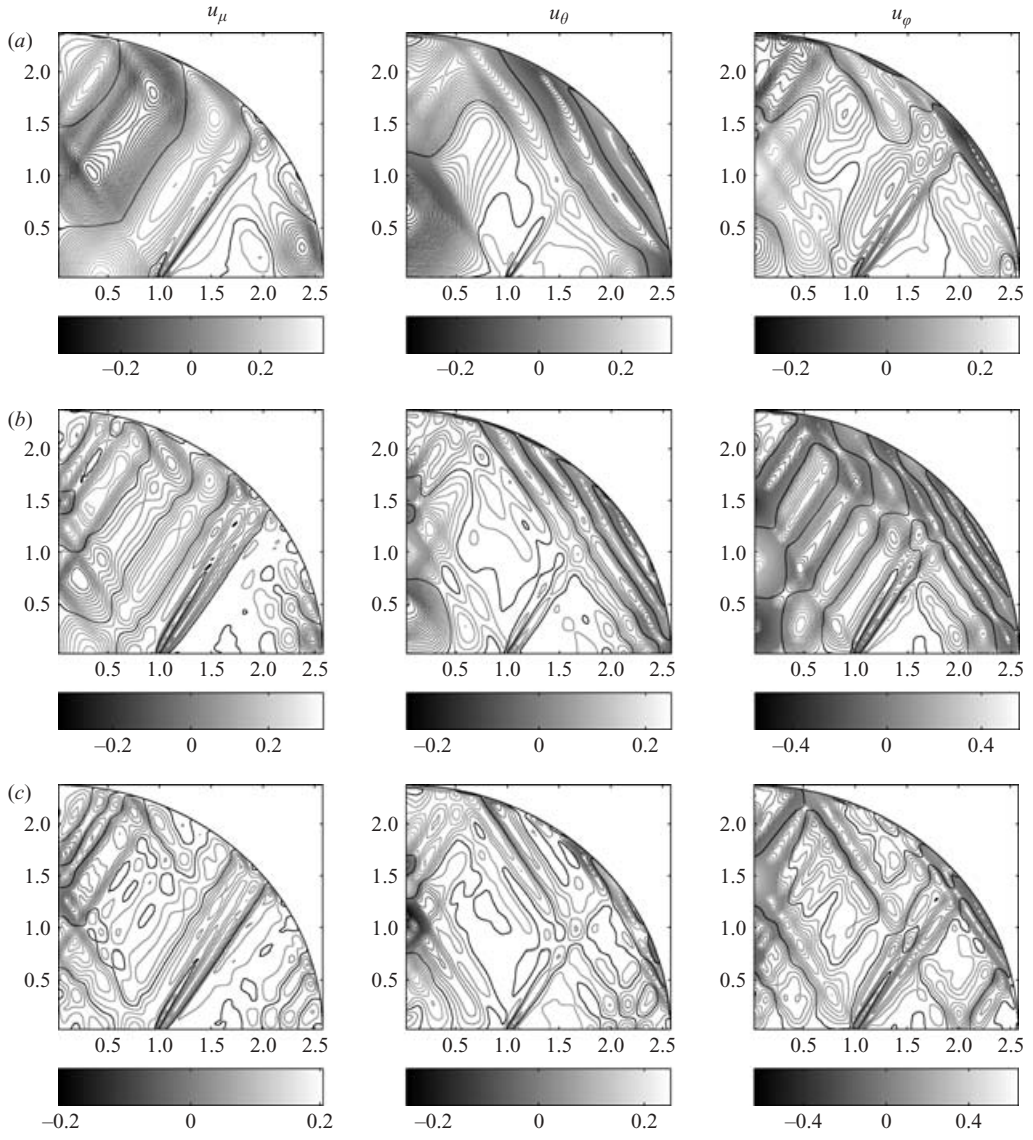

FIGURE 9. The three velocity components of the (8,1,5) (*a*), (14,1,9) (*b*) and (20,1,13) (*c*) viscous inertial modes within the meridional plane $\varphi = 0$, for $e = 0.39$; velocities are normalized so that $|\boldsymbol{u}|_{max} = 1$.

phenomena seem then to be present for these modes as for the spin-over one, but because several modes are involved in a limited eccentricity range, it may be difficult to associate precisely each anomaly with a given frequency crossing. To conclude, because of their proximity, several inertial modes enter into a resonance between each other through the viscosity, a behaviour more complex than expected in a simple non-viscous approach. As well, it is necessary to go beyond the first-order perturbation approach followed in the literature (Greenspan 1968; Zhang *et al.* 2004) to take these inter-mode resonances into account.

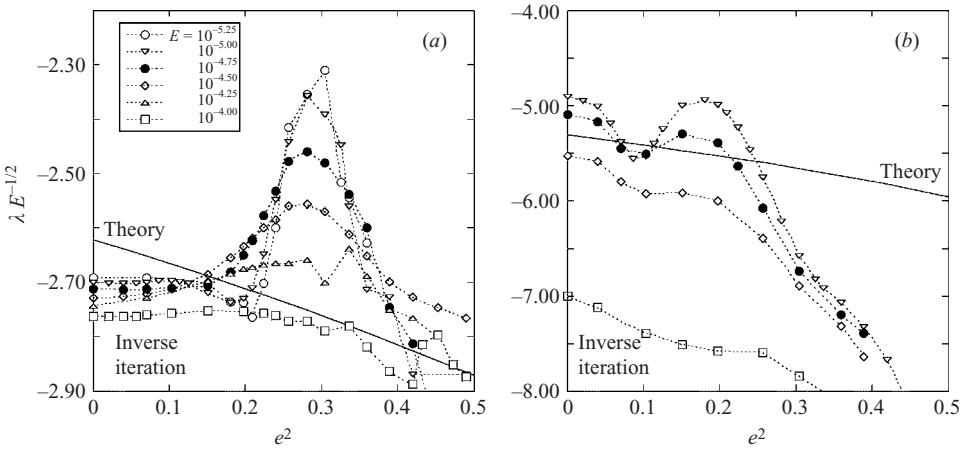

FIGURE 10. Eccentricity dependence of the renormalized decay factor $\lambda E^{-1/2}$ for (*a*) the (2,1,1) and (*b*) the (8,1,5) modes, for various Ekman numbers ranging from 10^{-4} to $10^{-5.25}$; continuous lines are theoretical predictions.

4.3. *Viscosity dependence of decay rates*

In order to better characterize how the decay rates are influenced by the viscosity, the (2,1,1) and (8,1,5) eigenmodes have been investigated by the inverse iteration method for several Ekman numbers (see figure 10). It appears that the anomalies occurring at the critical eccentricity become smoother as E increases, a behaviour characteristic of resonance phenomena. For a value of about 10^{-4}, they are almost completely damped and the theoretical variation is recovered. Note that the proximity of eigenfrequencies also means the proximity of boundary layer eruptions occurring at a critical latitude (see figure 5). It can be anticipated that these eruptions will play a crucial role in the viscous coupling between the corresponding modes, and that the amplitude of this coupling will depend on both the separation of the critical latitudes and the viscosity.

5. Discussion

In the present work, a detailed study of a few viscous $m = 1$ eigenmodes of a rotating fluid within a spheroidal container has been performed by direct numerical simulation. In a linear approximation, their behaviour, namely their viscous decay rate, the viscous correction to their eigenfrequency and their spatial structure, has been investigated as a function of the eccentricity e of the spheroidal container, for a Ekman number $E = 10^{-5}$. Particular attention has been paid to the spin-over mode, which plays a fundamental role in the precession problem. A main result is that a strong slowing-down of its viscous decay rate ($\sim$10 %) has been found in the range $e \approx 0.5$–0.6, shown by a large anomaly in its eccentricity dependence. This can be considered as the signature of a resonance between several viscous eigenmodes, in an eccentricity range where their frequencies become very close to each other. This resonance has not been predicted in previous linear theory (Greenspan 1968; Zhang *et al.* 2004). A higher-order perturbation analysis is needed to account for such an effect, by explicitly considering the coupling between different eigenmodes propagating at frequencies close to each other. However, the eigenfrequency spectrum is known to be dense, so that there are always many eigenmodes with a frequency close to that of a given mode. It can be assumed that a resonance between these modes could be

renormalized by a kind of coupling constant or interaction integral, which could be large only for a small number of pairs of modes. The magnitude of the decay rates, or the proximity of their value is probably also involved in the resonance phenomenon. Further analysis is required to elucidate this point. As well, the consequences of such a resonance for possible fluid instabilities remain to be investigated. Previous studies in spherical geometry have shown how the spatial structure of the spin-over mode changes as a function of the viscosity, i.e. how the internal shear layers scale with the Ekman number (Hollerbach & Kerswell 1995; Noir *et al.* 2001). One may wonder whether the same $E^{1/5}$ scaling applies to the present case with a large eccentricity, where the shear layers have been replaced by cell-like structures, at least for the E value used in the present calculation.

Most of the computations presented here have been performed at the *Institut du Développement et des Ressources en Informatique Scientifique* (IDRIS), under the project 41712.

REFERENCES

Backus, G., Parker, R. & Constable, C. 1996 *Foundations of Geomagnetism.* Cambridge University Press.

Busse, F. H. 1968 Steady fluid flow in a precessing spheroidal shell. *J. Fluid Mech.* **33**, 739–751.

Greenspan, H. P. 1968 *The Theory of Rotating Fluids.* Cambridge University Press.

Hollerbach, R. & Kerswell, R. R. 1995 Oscillatory internal shear layers in rotating and precessing flows. *J. Fluid Mech.* **298**, 327–339.

Kerswell, R. R. 1993 The instability of precessing flow. *Geophys. Astrophys. Fluid Dyn.* **72**, 107–144.

Kerswell, R. R. 1994 Tidal excitation of hydromagnetic waves and their damping in the Earth. *J. Fluid Mech.* **274**, 219–241.

Liao, X., Zhang, K. & Earnshaw, P. 2001 On the viscous damping of inertial oscillation in planetary fluid interiors. *Phys. Earth Planet. Inter.* **128**, 125–136.

Lorenzani, S. & Tilgner, A. 2001 Fluid instabilities in precessing spheroidal cavities. *J. Fluid Mech.* **447**, 111–128.

Lorenzani, S. & Tilgner, A. 2003 Inertial instabilities of fluid flow in precessing spheroidal shells. *J. Fluid Mech.* **492**, 363–379.

Noir, J., Jault, D. & Cardin, P. 2001 Numerical study of the motions within a slowly precessing sphere at low Ekman number. *J. Fluid Mech.* **437**, 283–299.

Poincaré, R. 1910 Sur la précession des corps déformables. *Bull. Astronomique* **27**, 321–356.

Rieutord, M. & Valdaretto, L. 1997 Inertial waves in a rotating spherical shell. *J. Fluid Mech.* **341**, 77–99.

Schmitt, D. & Jault, D. 2004 Numerical study of a rotating fluid in a spheroidal container. *J. Comput. Phys.* **197**, 671–685.

Stewartson, K. & Roberts, P. H. 1963 On the motion of a liquid in a spheroidal cavity of a precessing rigid body. *J. Fluid Mech.* **17**, 1–20.

Stoer, J. & Bulirsch, R. 1980 *Introduction to Numerical Analysis.* Springer.

Tilgner, A. 1999 Non-axisymmetric shear layers in precessing fluid ellipsoidal shells. *Geophys. J. Int.* **136**, 629–636.

Tilgner, A. & Busse, F. H. 2001 Fluid flows in precessing spherical shells. *J. Fluid Mech.* **426**, 387–396.

Walker, M. R. & Barenghi, C. F. 1994 High resolution numerical dynamos in the limit of a thin disk galaxy. *Geophys. Astrophys. Fluid Dyn.* **76**, 265.

Zhang, K., Liao, X. & Earnshaw, P. 2004 On inertial waves and oscillations in a rapidly rotating spheroid. *J. Fluid Mech.* **504**, 1–40.